

# A Comparative Study of the Electrical Properties of Undoped Schottky Junction In/A-Si:H/AZO-Coated-Glass and In/SiNWs/AZO-Coated-Glass Solar Cells

Abayomi Stephen<sup>1\*</sup>

<sup>1</sup>Independent researched, De Monfort University, United Kingdom

\*Corresponding author: Abayomi Stephen: abayomi.stephen@wiltshire.ac.uk



**Citation:** Stephen A. 2023) A Comparative Study of the Electrical Properties on Undoped Schottky Junction in/A-Si:H/AZO-Coated Glass and In/SiNWs/AZO-Coated-Glass Solar Cells. Open Science Journal 8(2)

**Received:** 14<sup>th</sup> February 2023

**Accepted:** 7<sup>th</sup> June 2023

**Published:** 30<sup>th</sup> August 2023

**Copyright:** © 2023 This is an open access article under the terms of the [Creative Commons Attribution License](#), which permits unrestricted use, distribution, and reproduction in any medium, provided the original author and source are credited.

**Funding:** The author(s) received no specific funding for this work

**Competing Interests:** The authors have declared that no competing interests exists.

## Abstract:

Plasma enhanced chemical vapour deposition (PECVD) is used to synthesise undoped hydrogenated amorphous thin film silicon (a-Si:H) and undoped silicon nanowire (SiNWs) array for solar cell applications. Indium metal is used as the top contact electrode in Schottky junction configured solar cells devices represented as In/a-Si:H/AZO-coated-glass and In/SiNWs/AZO-coated-glass respectively. For six solar cell devices on each sample, its observed that charge carrier trap states are observed under dark conditions, despite indium metal's farther position on the various impurities in silicon mid-band gap and minimum temperature for Vapour-Liquid-Solid (VLS) Silicon nanowire growth, which is expected not producing charge carrier trap states. In/SiNWs/AZO-coated glass solar device demonstrated non-rectifying and ohmic behaviour with no significant measurable solar cell device parameters, while In/a-Si:H/AZO-coated glass showed rectifying and Schottky behaviour with a reported average values of short circuit current ( $I_{SC}$ ) of  $(5.27 \pm 2.39)$ A, open circuit voltage ( $V_{OC}$ ) of  $(0.26 \pm 0.04)$ V, and ideality factor ( $n$ ) of  $(4.34 \pm 0.26)$ .

**Keywords:** Indium, PECVD, Hydrogenated amorphous silicon, Silicon nanowires

## Introduction

Schottky junction interfaces are employed in the fabrication of numerous devices. They have been the subject of extensive research and have found widespread application in electronic devices such as diodes, field effect transistors,

mixers, sensors, and solar cells (1-2). This widespread application can be attributed to the Schottky junction's simplicity and ease of fabrication in addition to its weak charge storage effect (1-4). The conventional Schottky junction devices is based on the physical interaction of metals like silver (Ag), gold (Au), copper (Cu), and platinum (Pt) and a layer of semiconductors materials such as hydrogenated amorphous silicon (a-Si:H), zinc oxide (ZnO), gallium arsenide (GaAs), indium phosphide (InP) etc. These Schottky junction based devices have the advantage of the metal layers with electron mobility far higher than that of semiconductor layers (5). More so, research done on silicon-based Schottky devices such as photo detectors reveals they offer low noise and quick signal response (6). In addition, research has demonstrated that certain silicon-based Schottky devices have additional benefits, including rapid charge carrier transit, mechanical flexibility, changeable work functions, and good optical transparency (7). Despite all the aforementioned properties, Schottky junction devices in general usually have problems, such as, sensitivity to the preparation methods and property degradation during the fabrication processes (8-9). In this work, studies have been conducted on the use of indium as top metal contact electrode for silicon-based Schottky solar cells fabricated by virtue of its distant position relative to silicon mid-band gap in Fig 1 below. The impurity level of indium metal is considerable distant of approximately -0.4eV from the middle bandgap of silicon (11-12) as seen in Fig 1. Its anticipated that with indium top metal contact electrode, better Schottky and rectifying characteristics due to less charge carrier traps states will be achieved occasioned by its distant from the middle band gap of silicon as seen in Fig.1. Indium and elements such as niobium, hafnium, gallium, germanium, iridium, tantalum termed Technology Critical Elements (TCE) are now employed in the manufacture of devices in telecommunications, electronic displays, semiconductors, and energy-related technologies (10) such as batteries.

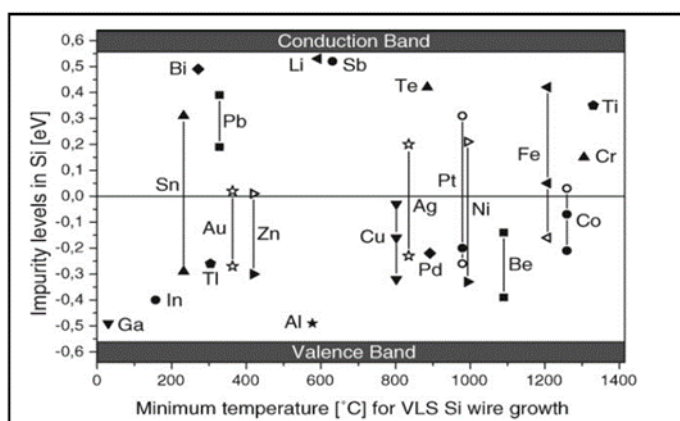


Figure.1 Impurity levels of various metals in silicon with respect to deposition temperature. Adapted from (1) and (11-12).

### *Indium as a technology critical element*

Indium is an essential element that is currently the subject of extensive research (10) for a diverse range of uses, as was noted previously in the preceding paragraph. Indium can be used as dopant in silicon based solar cells, catalyst for the growth and synthesis of nanowires and contact electrodes for various electronic and solar cell applications. Indium is frequently combined with other elements that are found

in oxide form with other elements like tin, which results in the formation of the semiconducting material known as tin doped-indium-oxide (ITO). This material is utilised as contact electrodes and/or in other instances as semiconductor active layers in a wide variety of electronic, energy producing, and opto-electronic applications. An investigation of several of these devices, focussing on the advantageous and disadvantageous features of each one in particular are discussed in brief. The use of amorphous indium-gallium-zinc oxide (IGZO) as the semiconducting layer, of which indium and gallium are TCE, was used for the manufacture of mechanically flexible mobile phones with fast processing speeds of about 6.3 GHz for wireless communication applications (13). This was established by investigating the prospects of indium-based materials for the fabrication of Schottky junction diodes on plastic substrates (13). In the fabrication of this Schottky diode device, these researchers were able to achieve low signal losses at high frequency. In the electrical characterization that was performed by applying the current-voltage (I-V) measurement method, a dc bias voltage of 1-V was applied across the Schottky diode device, which resulted in varying turn on voltages ranging from 0.8V, 1.2V, and 1.6V with respect to the mass thickness of the IGZO layers of 50nm, 80nm, and 100nm respectively (13). In this particular device, the ohmic contacts electrodes are made from aluminium (Al) metal, whereas, the non-ohmic/Schottky contact electrode are made of platinum (Pt). This Schottky diode device under study consisted of indium metal combined with a number of different semiconductor materials reported higher turn-on voltages however, a major challenge is the fabrication process takes time coupled with added cost of the materials. More research into the utilisation of indium-based materials to study the photovoltaic effect on bismuth ferrite ( $\text{BiFeO}_3$ ) thin films (14) as the semiconducting layer with ITO as the top metal contact electrode and a bottom metal contact electrode of strontium ruthenate ( $\text{SrRuO}_3$ ) is characterised by open-circuit voltages 0.8–0.9V and external quantum efficiencies of up to 10% when illuminated with light. The efficiency report is at least an order of magnitude higher than the maximum efficiency when exposed to sunlight at the (AM1.5) condition. In spite of the high efficiency and high open circuit voltage, this particular device has a significant obstacle on account of the heterostructure design in that, good lattice matching must be achieved for optimal performance of this device. This is a fundamental prerequisite for the creation of high-quality heterojunctions (15). In order to satisfy this criterion, it is necessary for the lattice constants of all of the participating semiconductor materials be as close to each other as possible which is challenging. Another group of researchers (16) investigated wide-band-gap chalcopyrite solar cells made up of copper, indium, gallium, and selenium ( $\text{Cu}(\text{In,Ga})\text{Se}_2$ , also known as (CIGS), and silver, copper, indium, gallium, and selenium ( $\text{Ag,Cu}(\text{In,Ga})\text{Se}_2$ , also known simply as (ACIGS), both of which had ITO transparent back contact electrodes respectively. They found that these indium-based oxides prevented sodium from diffusing into the active semiconducting layer of each device. This led to solar cell efficiencies of 12% when using ITO/ACIGS and 11.2% when using ITO/CIGS respectively (16). As such, there is a large quantity of materials required to achieve such efficiencies, which tends to increase the complexity of the fabrication process. This is particularly problematic if the materials are chemically synthesised, and in addition, the appropriate lattice matching must be realised which is vital criteria for heterostructure devices. More research conducted on indium based material (17) also reveals the infusion of twenty layers of indium based quantum dots, a Schottky barrier solar cell with indium-arsenide ( $\text{InAs}$ ) quantum dots inserted into the active semiconducting layer composed of GaAs with a contact electrode at the top of ITO

results in an increase of both the open-circuit voltage and the short-circuit current density. In addition to this, it has been reported that both the photoluminescence and the external quantum efficiency was greatly improved (17). As stated above, complexity of the fabrication process, time it takes to fabricate these devices and increased material cost are the challenges faced in making these devices. We propose the use of indium as a single element for use as the top metal contact electrode for two categories of Schottky junction-based solar cell devices, namely undoped In/a-Si:H/AZO-coated-glass and undoped In/SiNWs/AZO-coated-glass, because the location of indium is far and distant in relation to the impurity levels of various metals in silicon mid-gap with respect to deposition temperature chart as earlier shown in Fig.1 above. Consequently, it is anticipated that this will not create trapped states in the lattice of the devices when they are fabricated in solar cell devices and could result in enhanced performance devices. Moreover, this particular structural arrangement, which is made up of undoped Schottky junction solar cells, has not been the subject of substantial investigation. Additionally, the simplicity of fabrication, low material usage and ease of characterisation were very expensive instruments are not required for measurements are some of the benefits of making these devices. Furthermore, very extensive research has shown that silicon-based doped heterojunction planar, thin film devices (18-20) and silicon-based nanostructured devices (21-22) respectively composed of indium-based materials either as active semiconductor layer, contact electrodes, or front and rear trapping structures present average efficiencies values of approximately 23.6%, 7.8%, and 10.6% respectively. When all of the processing conditions are fully optimised (23), it is hoped that the preliminary investigations into fabrication and subsequent comparative study of the electrical properties of undoped In/a-Si:H/AZO-coated-glass and undoped In/SiNWs/AZO-coated-glass in this paper will serve as the stepping stone to further studies with the objective of achieving a simple device with enhanced external quantum efficiency (EQE). In the succeeding sections, more discussions regarding the procedure that was utilised for fabricating these devices, as well as the materials that were utilised, the methods of characterisation, the results, and the conclusions are presented.

## Materials and methods

In recent years, the most common method for depositing a-Si:H and VLS synthesised SiNWs has been through a process known as radio-frequency PECVD (11-12) (24). The deposition process is such that a gaseous silicon precursor gas known as silane ( $\text{SiH}_4$ ) in the presence of hydrogen ( $\text{H}_2$ ) gas is subjected to electron impact dissociation and a secondary induced chemical reaction ultimately results in the deposition of silicon layers on the target substrates and the formation of undoped a-Si:H thin film layers and undoped SiNWs growth in the presence of a metal catalyst respectively (11) on Aluminium doped Zinc oxide coated glass (AZO-Coated-Glass). The deposition process and synthesis of SiNWs is further explained in section 2.1 of this paper. The comparatively low deposition temperature requirement of the PECVD technique constitute a considerable benefit of using this technique for the fabrication of semiconductor devices. Consequently, PECVD makes it possible to fabricate solar cells and other electronic devices using low-cost substrates that can be heated to temperatures typically between 200°C and 300 °C (24-26). Some disadvantages of PECVD is relatively low deposition rate typically ranging between 0.1-0.3nm/s and sometimes the creation of pinholes

on the semiconductor absorber layers in this case, undoped a-Si:H and SiNWs array (24 and 28). In spite of the low deposition rate associated with PECVD, it is possible to achieve good quality a-Si:H thin film and SiNWs array exhibiting good electrical and transport properties just by tweaking and adjusting process parameters during the deposition and synthesis. The choice of AZO-coated-glass as the bottom contact electrode of all devices in this paper is based on the prominence gained in the fabrication of flat panel displays, electroluminescent and solar cell devices due to numerous properties as its ability for high optical transmission in the visible range of 400-700nm, wide band gap of 3.3eV, good electrical conductivity of  $10^4 \text{ Scm}^{-1}$  and most especially its stability in plasma (29-32). The structural configuration of these solar cell devices fabricated in this work are displayed in Figs. 2 and 3 of section 2.1 respectively.

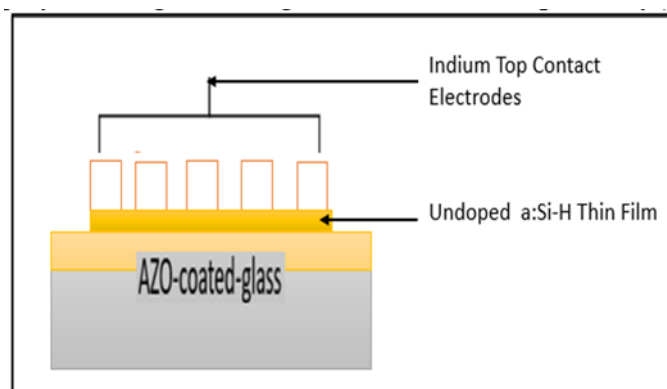


Figure 2 The structural 2-D configuration of Schottky junction In/a-Si:H/AZO-coated-glass solar cell.

### *Silicon nanowire growth and synthesis*

The standard laboratory cleaning techniques was used to clean samples of AZO-coated glass and Corning glass 7059. The cleaned samples for undoped a-Si:H contained no thermally evaporated tin metal catalyst. Thermal evaporation of a 5nm mass thickness of tin metal catalyst on AZO-coated glass and Corning glass 7059 were all exposed to plasma pre-treatment for 2 minutes at a  $\text{H}_2$  flow rate of 100sccm at a pre-set temperature of  $300^\circ\text{C}$  and pre-set chamber pressure of 500mTorr. PECVD technique was used for VLS synthesised tin catalysed SiNWs at a  $\text{H}_2/\text{SiH}_4$  dilution ratio of  $R = 5:1$  for 30 minutes at a radio frequency of 13.56MHz. A deposition temperature and chamber pressure of  $300^\circ\text{C}$  and 900mTorr were set respectively. Indium metal top contact electrode was thermally evaporated on samples of undoped a-Si:H layer and undoped SiNWs grown on AZO-coated-glass with a mass thickness of 120nm to complete the device fabrication process

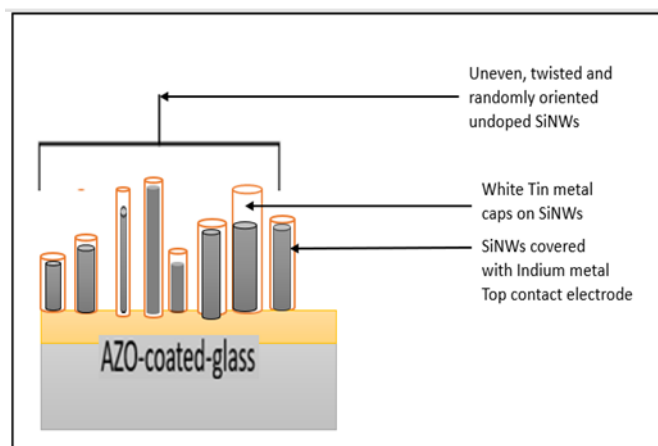


Figure.3 The structural 2-D configuration of Schottky junction In/SiNWs/AZO-coated-glass solar cell

## Device characterisation

The structural, optical and electrical properties of undoped a-Si:H thin film and undoped SiNWs arrays are then investigated in this section. Analyses and characterisations of the morphology of undoped a-Si:H and undoped SiNWs deposited on AZO-coated glass and optical properties on Corning glass 7059 respectively, were conducted using Scanning Electron Microscopy (SEM) technique and Ultraviolet and Visible (UV-Vis) spectroscopy. The latter characterisation method was used to determine and estimate the band gap ( $E_g$ ) of these semiconductor absorber materials. Electrical characterization of solar cell devices fabricated that is, undoped a-Si:H thin film and undoped SiNWs array after thermal evaporation of indium top metal contact electrodes was carried out with a Hewlett-Packard (4140B) Pico-ammeter-meter that was coupled to a solar simulator. The solar simulator was equipped with an Oriel 96005 illumination solar simulator, 150W from Newport, and filters that were designed to give an output power density of  $1000\text{W}/\text{m}^2$  or  $100\text{mW}/\text{cm}^2$  when AM1.5 standard test conditions (STC) are set. Current-voltage (I-V) measurements was carried out by establishing a direct current (dc) voltage of 1V across each set of devices with a 10mV step size with connection shown in Figs.4a and 4b below. This was done in order to compare the electrical properties of both types of Schottky junction solar cell devices.

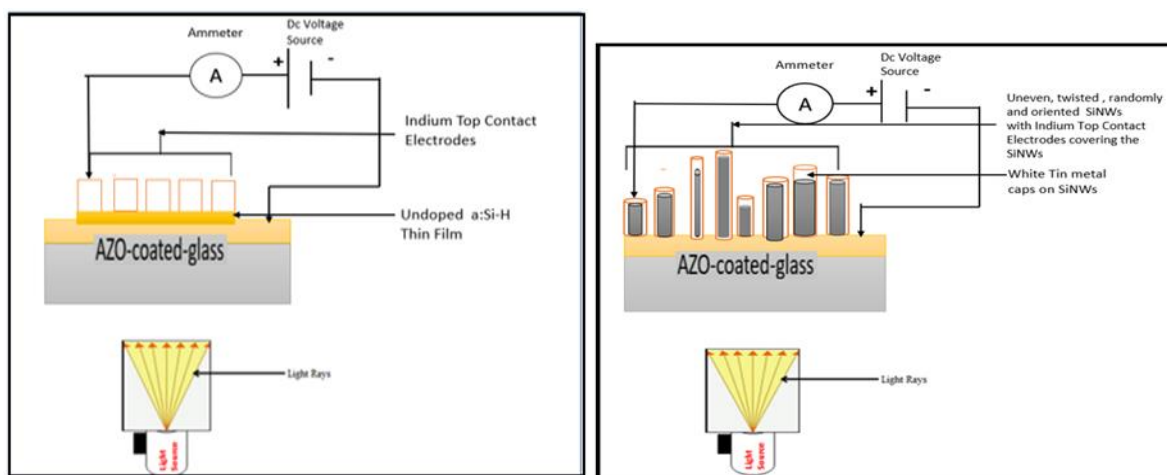


Figure.4(a) Shows the structural and the electrical biasing configurations for the current voltage I-V measurements of Schottky junction undoped In/a-Si:H/AZO-Coated-Glass on the left and Fig.4(b) undoped In/SiNWs/AZO-Coated-Glass on the right solar cell devices respectively.

## Results and discussion

This section discusses the results of characterization and measurements after the devices have been fabricated. These data were collected after the devices were measured under STC mentioned above.

### *Structural characterisation*

Fig.5 contains micrographs taken with a scanning electron microscope (SEM) of an undoped a-Si:H thin film layer. According to the reports (33-35), light scattering is enabled in thin film a-Si:H due to surface roughness morphology of AZO-coated-glass (36) on which a-Si:H thin film is deposited. In addition, tiny islands of a-Si:H thin film are observed, which also mimics the surface roughness morphology of AZO-coated glass. Furthermore, the non-uniformity in the a-Si:H thin film and the creation of pinholes going down the AZO-coated-glass surface are typical for a-Si:H deposited through PECVD method (28) and (36-37).

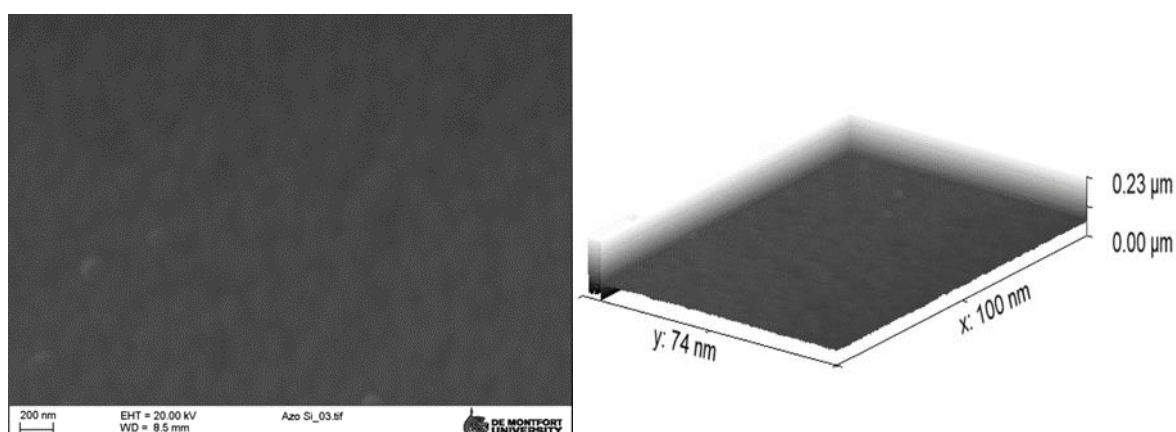


Figure.5(a) Shows the morphologies of undoped a-Si:H SEM micrographs in 2-D on the left and Fig.5(b) 3-D and on the right respectively.

Next we discuss the image of the SEM micrograph of undoped SiNWs array is shown below in Fig.6. The undoped SiNWs array are composed of highly disordered, randomly aligned and oriented SiNWs array composed of twists and kinks between each adjacent SiNWs. Variations in diameter, pitch, and length exist around the average values of SiNWs arrays synthesised using VLS techniques are characteristic of these kinds of nanowires (38-41). After the growth of these SiNWs, the formation of white caps with rounded tops as observed in Fig.6 and this is an indication of Tin metal catalyst residue from SiNWs synthesis process.

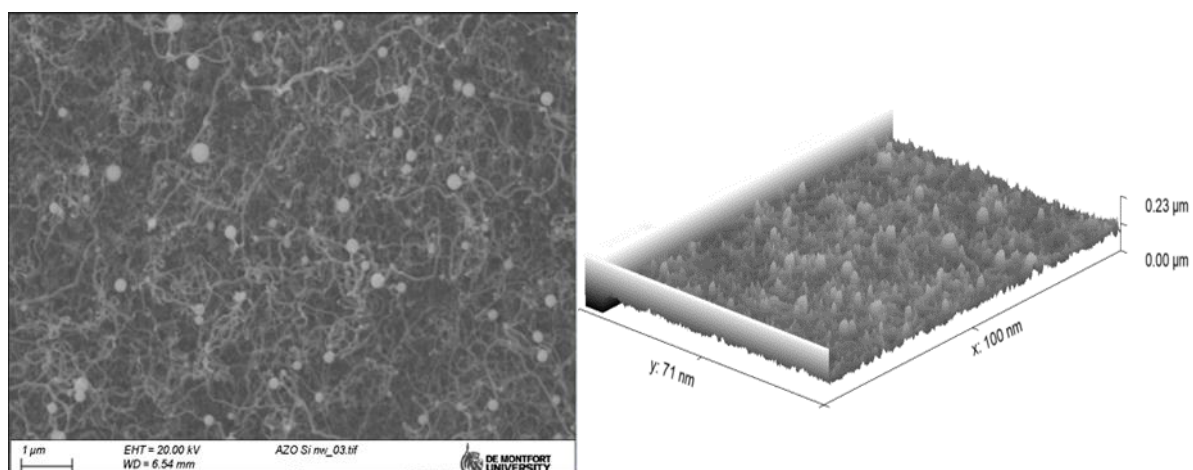


Figure.6(a) Shows the morphologies of undoped SiNWs SEM micrographs in 2-D on the left and Fig.6(b) 3-D and on the right respectively

SEM technique was used above, to investigate the surface topography of materials at both the nano and micro scales. This is accomplished by making use of focussed beams of electrons that are generated by a metallic filament through either the thermionic emission or field emission of a cathode. Using SEM, it is amazingly simple to obtain a picture of a rough two or three-dimensional object at a low magnification less than 1000x (42). This method of characterisation has a controllable energy range that can go anywhere from 100eV-30KeV, thus, in this paper, the Zeiss Evo 15, Leica S430 model at an accelerating voltage of 20KV with an accuracy working distance (WD) of 8.5mm and 6.54mm at a tilt angle of 45°, coupled with image resolutions of 200nm and 1μm for both undoped a-Si:H thin film and undoped SiNWs arrays respectively has been used to characterise all the samples (42-43). The images obtained from these samples can be seen to bear close semblance and agreement to what has been obtained in literature (26-28) and (38 and 41). The major limitation of SEM imaging is low magnification compared to Transverse electron microscopy (TEM). As such, some margin of error in structural characterisation is acknowledged in this work.

### *Optical characterisation*

Optical characterisation process works on the principle of the absorption of electromagnetic energy with an electronic transitional motion of molecules, creating an excitation effect on these electrons from an occupied to an unoccupied energy state or level (44). Infrared absorption corresponds to molecular vibrations within the substrate or semiconductor material. The optical band gap is eventually derived by extrapolating the linear portion of the graph to find the corresponding value of

energy ( $E$ ), at  $(\alpha E)^x = 0$ , which is the intercept on the x-axis at  $y=0$ . The absorption coefficient is represented as  $(\alpha)$ . Silicon based materials are indirect band gap semiconductors (44-45), the value of  $x = 0.5$ . The optical properties of undoped a-Si:H and undoped SiNWs are investigated in this sub section and compared in Figs.7a and 7b.

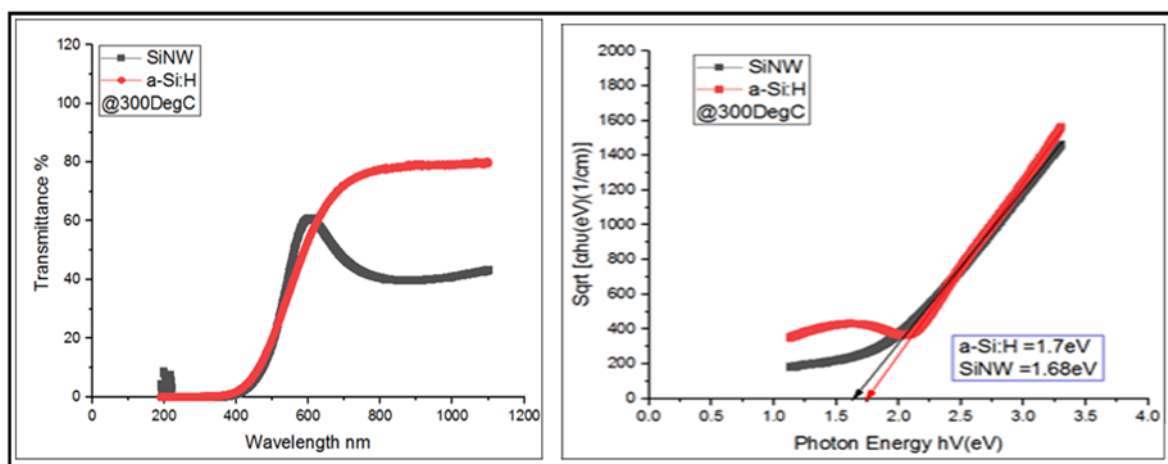


Figure.7(a) Shows the plot of Transmittance vs Wavelength and 7(b)  $\sqrt{\alpha h\nu}$  vs Photon energy of undoped SiNWs and undoped a-Si:H thin film are compared.

The absorption peaks of undoped a-Si:H thin films seen in Fig.7a are consistent with reported literature (45-46). Undoped a-Si:H thin films exhibit clear evidence of absorbing light in the ultraviolet region of the spectrum all the way up to a peak value of 600nm. There is a direct correlation between the maximum absorption rate and a transmittance rate of 60%. In the portion of the electromagnetic spectrum known as the near infrared, optical absorption begins to diminish about 800nm, although transmission remains essentially and fairly at a constant level all the way up to 1100nm. This is because near infrared light has a shorter wavelength than longer infrared light. The optical band gap is more accurately determined from reflection and transmission measurements using the Tauc plot (44) as shown in Fig.7b.

Similarly, in Fig.7a, SiNWs array have a darker surface under visible light, because they are able to absorb light with wavelengths up to 620nm over the whole UV spectrum (47). As a consequence of this, the SiNWs array exhibits decreased reflectance and increased absorbance; more specifically an absorption of around 64% in the visible region is observable. There is a possibility that disordered randomisation of SiNWs and its directional alignment within the SiNWs array is a reason for the increased maximum transmittance levels of the SiNWs array (47-49). Regardless of the growth and synthesis method, the optical properties of nanowires in general, may be described using UV-Vis measurements and optical band gaps estimated from Tauc plots (44 and 46). As such, in this work, we have obtained the optical characteristics of the samples by using the Shimadzu UV-3600i Plus UV-Vis spectrophotometer machine which contains a high-performance, grating-grating double monochromator, and accomplishes a low stray-light level while maintaining a high resolution. The range of wavelengths extends from 185-3300nm. This apparatus is capable of performing spectrophotometry on a wide variety of samples, including those that call for high resolution, like gas samples, as well as those that are highly concentrated in liquid form. In UV-Vis measurement, the transmittance  $T\%$  is computed using the Beer Lambert

expression in equation 1, in which an absorbing material with equal thickness is believed to have equal radiant energy traversing it as described below by the list of equations 1-5.

$$I_T = I_0 e^{-\alpha d} \quad [1]$$

$$\frac{I_T}{I_0} = T \quad [2]$$

$$\%T = \frac{I_T}{I_0} \times 100 \quad [3]$$

$$A = \log_{10} \frac{I_0}{I_T} \quad [4]$$

$$R = 1 - A - T \quad [5]$$

Where,

- $I_0$  is the intensity of the incident radiation.
- $I$  is the transmitted light intensity.
- $T$  is the transmittance.
- $A$  is the absorbance.
- $R$  is the reflectance.
- $\alpha$  is the absorption coefficient in ( $\text{cm}^{-1}$ ).
- $d$  is the thickness of the absorber layer in (cm).

It is essential to remember that incident radiation from the UV-Vis spectrophotometer influences the amount of radiant energy that travels through samples of undoped a-Si:H thin films and undoped SiNWs array under test having given thin film and nanowire approximate thicknesses ( $d$ ) of 70nm and 250nm respectively as obtained from profilometer measurements not shown here due to faulting interface cables to extract the data in excel spreadsheet form. The absorbance of the silicon structures created for the investigation undoped a-Si:H thin films and undoped SiNWs arrays were calculated using Equation 5.3 above. While transmittance is typically expressed as a percentage, there are no units for absorbance (50). Then the optical band gap describing the optical properties of the solar cell devices are calculated using UV-Vis data displayed on the graphs in Figs 7a and 7b. Based on UV-Vis measurements, Fig.7b presents the optical band gap measurement values of undoped a-Si:H and undoped SiNWs array respectively, having values of 1.68 and 1.70eV. When compared to undoped a-Si:H thin film, the optical band gap value that was reported and obtained is indicative of the fact that, undoped SiNWs arrays synthesised in this work, appear to exhibit a considerable amorphous behavioural phase which appears to be in agreement with studies carried out by (51-52). Further verification from X-ray diffraction (XRD) characterisation in Fig.8 below appears to support this notion.

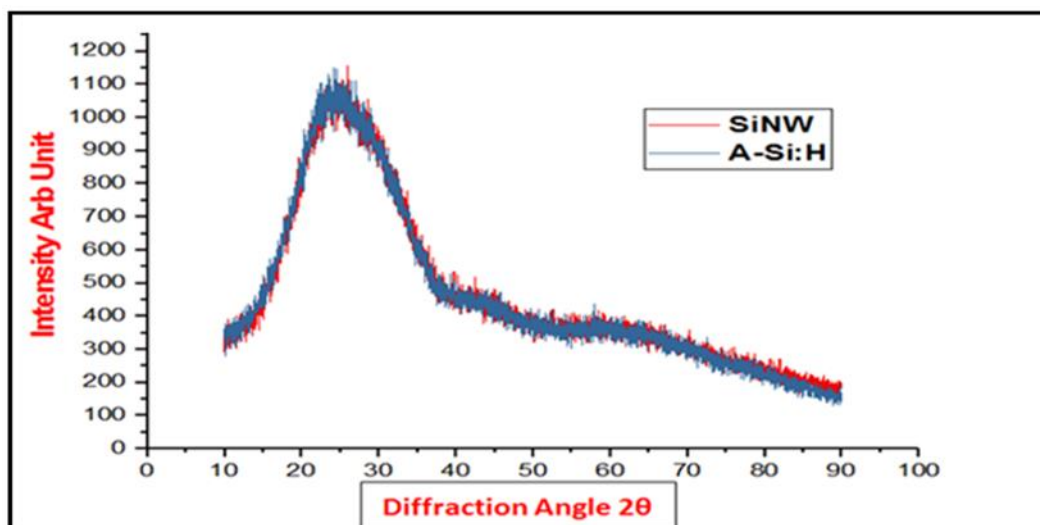


Figure.8 The XRD patterns of undoped a-Si:H thin film and undoped SiNWs array measured is compared.

All XRD measurements of undoped a-Si:H thin film and undoped SiNWs array in this paper was carried out using the Bunker D2 Phaser equipment. The equipment has a one dimension (1-D) Lynx detector and  $0.02^\circ$  resolution angle was utilised to scan the samples. The examinations were conducted with the aid of a copper anode to generate monochromic X-rays between nickel filters at 1.54 wavelengths with an accelerating voltage of 30KV and current flow of 10mA. Thus, from Fig.8 above, its noticeable that undoped a-Si:H thin film and undoped SiNWs array both have their 2 theta-points ( $2\theta$ ) occurring between  $25^\circ$  and  $27^\circ$  respectively. The XRD plot further indicates that there are no visible crystalline silicon sharp peaks; rather, the diffraction pattern produced for both semiconductor material exhibits a peak broadening suggestive of amorphous shell structure (51). XRD is a technique for studying the crystalline structure and crystal phases of a material. This is done so as to comprehend the crystallinity of an amorphous, polycrystalline, or monocrystalline semiconductor sample. By measuring the intensities and scattering angles of the X-Rays emitted from within the atoms of the material under test, the crystalline structure can be determined. Interactions between the X-Rays and the atoms of the sample are predominant enough to produce constructive interference of diffracted waves according to Bragg's Law, i.e.  $n\lambda = 2d\sin\theta$ . When samples are surveyed over a range of values known as  $2\theta$  points. The inbuilt software collects and processes a number of diffraction patterns (53-54). The peaks indicate the crystallinity of the material. According to multiple sources, the peak width is inversely proportional to crystal size and directly proportional to the diffraction angle, i.e.  $2\theta$ . It is vital to realise that no characterisation technique can be considered flawless. Therefore, it is appropriate to recognise the possibility that specific mistakes in characterisation may have arisen in this study, particularly in relation to the optical characterisation of the samples under investigation, namely undoped a-Si:H thin films and undoped SiNWs array. The investigation from (55) has revealed that UV-Vis, which was utilised to establish the optical band gap, has been documented to possess certain limitations. Stray lights, arising from imperfect wavelength selections, can lead to the transmission of a small amount of light across a wide range of wavelengths from the light source. This can potentially introduce substantial inaccuracies in measurements. Furthermore, the phenomenon of light scattering can introduce a certain degree of uncertainty in measurements. Additionally, if the components of

the instrument, namely the cuvette that holds the sample, are not properly positioned due to geometrical considerations, the obtained results may be inaccurate (55). It is sufficient to accept that a margin of error may have occurred due to the usage of a glass substrate containing silicon as opposed to GaAs to provide a more definite XRD measurement (54 and 56).

### *Electrical characterisation*

The following sections will present the electrical biasing configuration, band diagrams, and current-voltage (I-V) characteristic curve measurements for undoped Schottky junctions In/a-Si:H/AZO-coated-glass and In/a-SiNWs/AZO-coated-glass solar cell devices. The focus of this article is centred on the comparative investigation of the electrical properties demonstrated by these semiconductor devices. This study provides a thorough examination of the approach utilised in determining the essential circuit and device parameters of Schottky junction solar cell devices. To perform this, it's important to establish the theoretical working principles of Schottky junction device which is already well established from the knowledge gained in semiconductor physics and extensively researched by many scholars (56-60). The choice of Schottky solar cells is influenced by their simple fabrication procedure, coupled with low material costs in comparison to alternative silicon structures such as pn and p-i-n architectures (60-61). The Schottky junction solar cell can be regarded as a majority carrier device due to the absence of minority carrier injection at its junctions (56-57). The formation of a junction occurs when a metal and semiconductor layers are electrically in contact. The behaviour of the junction is dependent upon the characteristics of the interface, that is either Schottky or Ohmic which are primarily determined by the work function and electron affinity of the metal and semiconductor respectively (56-57). Furthermore, the presence of surface states can also exert an influence on the characteristics of the junction that is established. Currently, Schottky junction solar cells offer a notable benefit compared to pn junction solar cells. This advantage includes a lower forward turn-on voltage, in addition to the relative simplified structural architecture. Fig.9 seen below illustrates the schematic structural diagram of a conventional n-type Schottky junction solar cell.

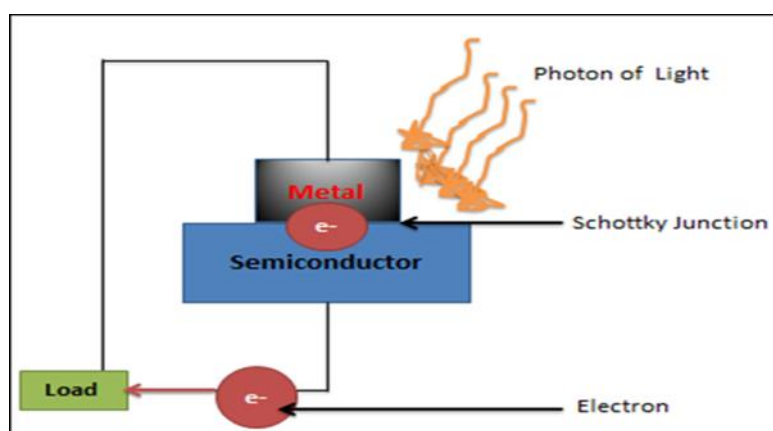


Figure.9 Schematic diagram of a n-type Schottky junction solar cell showing the flow of electrons to the external load represented by the green rectangle adapted from (57) with photons of light shone at the metal and semiconductor junction to facilitate electron flow.

The principle of operation of Schottky solar cells involves the generation of electron-hole pairs (EHP) at the Schottky interface when photons with energy exceeding the semiconductor's band gap are absorbed by the device. This leads to the separation of charges within the device. The migration of minority carriers, specifically holes (h), into the metal region has a broad impact, leading to the accumulation of charge in the semiconductor due to the presence of majority carriers that remain in the material. The quasi-Fermi level of the majority carriers in the semiconductor exhibits a tendency to shift, as illustrated in Fig.10. It is noteworthy that in the case of an n-type semiconductor seen below, the quasi-Fermi level of the electrons is positioned at a certain distance from the junction and experiences an increase in magnitude with the intensity of illumination. The quasi-Fermi level exhibits an elevation relative to the Fermi level of the metal. A photo-voltage is thereby produced in the external load connected to the solar cell, due, largely to the splitting of the Fermi energy level (57). The tendency of the semiconductor layer to sustain the difference in the quasi-Fermi level in the Schottky junction is crucial to maintaining the photovoltaic to electrical energy conversion.

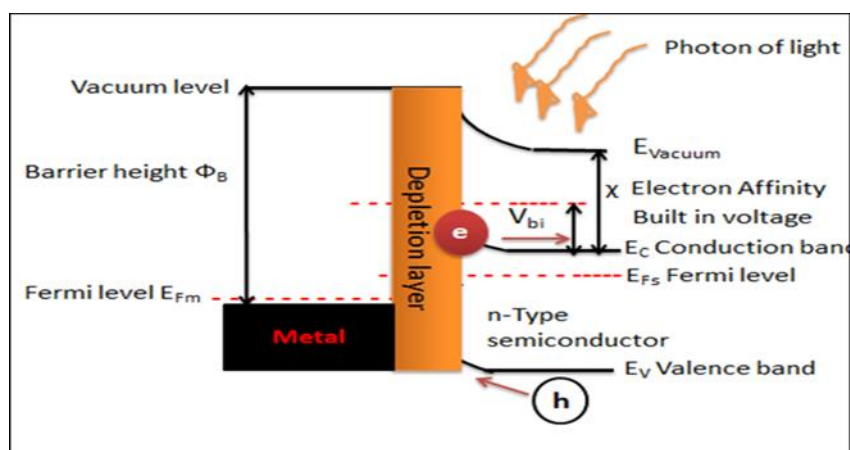


Figure 10 Simplified band diagram of a metal and n-type semiconductor Schottky solar cell depicting the thermionic emission across the Schottky junction under illumination condition adapted and drawn from (57).

At thermal equilibrium, the contact potential between metals and semiconductors establishes a state of charge carrier transport equilibrium, resulting in a net current flow of zero. In order to comprehend the current-voltage (I-V) behaviour of Schottky junctions, it is necessary to examine two distinct circumstances. The conditions being referred to are forward and reverse voltage bias. The magnitude of the current is contingent upon the specific biasing conditions and the level of external voltage applied (58-59). In the context of a metal-and n-type semiconductor diode operating under forward bias, the semiconductor layer is electrically connected to the negative voltage, while a positive voltage is applied to the metal layer. The external voltage acts in opposition to the inherent voltage present across the depletion layer. Consequently, the Fermi levels are no longer in a state of equilibrium, but rather exhibit a shift relative to each other, contingent upon the magnitude of the applied voltage, as depicted on the left side of Fig.11.

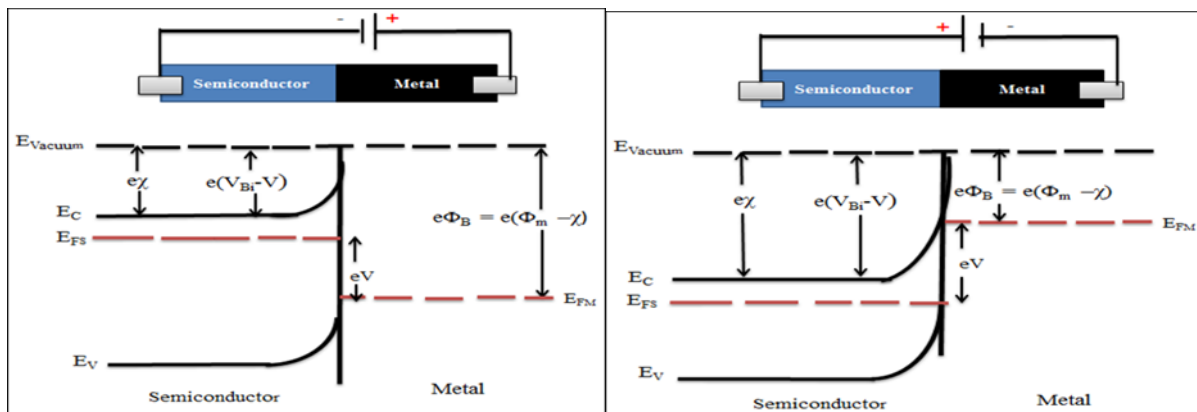


Figure.11(a) Metal and n-type Schottky junction solar cells in positive DC voltage bias and Fig.11(b) negative DC voltage bias conditions on the left and the right respectively adapted from (58), also indicating the metal work function ( $\Phi_M$ ), electron affinity ( $\chi$ ), barrier heights ( $e\Phi_B$ ), built-in-voltage ( $V_{Bi}$ ), conduction band ( $E_C$ ), valence band ( $E_V$ ), metal fermi-level ( $E_{FM}$ ), semiconductor fermi-level ( $E_{FS}$ ) and applied voltage ( $eV$ ).

### *Current-Voltage (I-V) measurements on solar/photovoltaic cells.*

Solar cells are devices that convert light energy into electrical power through the use of semiconductor materials, such as pn junction devices or metal-semiconductor materials like Schottky junction devices (56-60), as explained in the field of semiconductor physics and physics of solar cells (62). The process of electrically characterising solar cells involves the measurement of current and capacitance in relation to the applied direct current (dc) bias voltage (63). Typically, the I-V measurements for solar cells are conducted in accordance with standard testing conditions (STC). These circumstances involve testing the solar cell devices under an air mass (AM 1.5) spectrum, while maintaining a solar cell temperature of 25°C, and exposing them to an irradiance power density of 1000W/m<sup>2</sup> or 100Mw/cm<sup>2</sup>. Hence, the assessment of the electrical properties of solar cells performs a pivotal role in the determination of their effectiveness and the development of approaches to minimise energy dissipation in these solar devices. In this work, the usage of the Hewlett-Packard (4140B) Pico-ammeter-meter in combination with the Oriel 96005 illumination solar simulator, a 150W device manufactured by Newport, and filters that have been specifically built for this purpose. (63). These equipment's are made up of software, mathematical analysis capabilities and graphics to obtain the I-V curves shown later in Fig.13 and Fig.15 of sections 3.3.2 and 3.3.3 respectively. A commonly used electrical representation of a solar or photovoltaic cell array is an equivalent electrical model, as depicted in Fig.12. The model consists a current source ( $I_L$ ) generated through the optical absorption of photons incident on the solar cell. This current source is connected in parallel with a diode that mimics the actual solar or photovoltaic cell array. The diode produces a current ( $I_s$ ) due to diode or reverse saturation. The model contains two distinct types of resistances, specifically a series resistance ( $R_s$ ). This resistance is indicative of various factors, namely; metal contact electrodes, ohmic losses occurring in the cell front or top surface, junction depth, and concentration of impurities (64-65). The presence of  $R_s$  in a solar cell has the effect of decreasing the short circuit current ( $I_{sc}$ ), thereby leading to a reduction in the maximum power output of the solar cell. Minimising  $R_s$  in solar cells is desirable. In contrast, the shunt resistance ( $R_{sh}$ ) characterises the undesired current leakage occurring at the periphery of the solar cell or as a result of crystal defects within

the cell. Ideally, it is desirable for the resistance value of  $R_{sh}$  to be significantly large or approaching infinity from studies conducted by (64-65). As such, there is a direct relationship between the  $R_{sh}$  and the open circuit voltage of the solar cell (65-66).

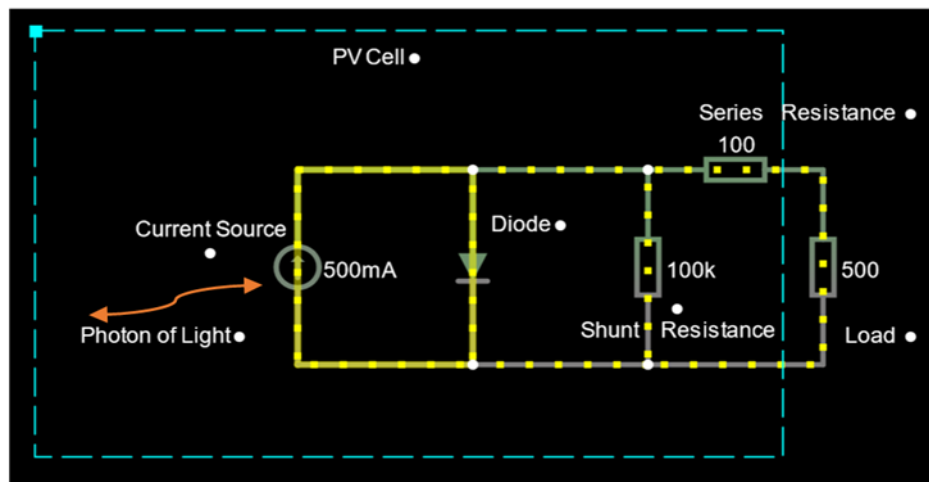


Figure.12 Shows an equivalent electrical model of a solar/photovoltaic cell array with some randomly selected current source and series, shunt and load resistance values which are adapted from (64) indicative of some solar cell parameters drawn with falstad software.

Equation 6 seen below elucidates the correlation between the total current ( $I$ ) flowing through the circuit in the presence of a load resistor coupled to an illuminated solar or photovoltaic cell array. The characterization and measurement of the current-voltage ( $I$ - $V$ ) relationship provide essential electrical parameters that are utilised to estimate the efficiency ( $\eta$ ) of the solar cell.

$$I = I_s \exp \left[ \left( \frac{eV}{nkT} - 1 \right) \right] - I_L \quad [6]$$

From the equation 6,  $n$  is a figure of merit called ideality factor ( $n$ ) which is dependent on the solar cell temperature. For silicon based solar cells, a good  $n$  is between 1 and 2, with 1 been the best ideality factor of a high performing solar cell (66-67). The thermal voltage at equilibrium is defined by  $kT/e$  which is approximately 0.0257volts for which  $k$  is referred to as the Boltzmann constant that relates energy to temperature in a system (solar or photovoltaic cell array) with an approximate value of  $1.38 \times 10^{-23}$  joules per kelvin and  $e$  depicts electron charge which is  $1.6 \times 10^{-19}$  coulombs. The voltage  $V = 1V$  across the diode or solar cell in this instance (68) is also depicted in the equation. The maximum power point ( $P_{max}$ ), which is determined by the product of the maximum current ( $I_{max}$ ) and the maximum voltage ( $V_{max}$ ) obtained as the area under the curve shown by the shaded black rectangle from a typical forward bias  $I$ - $V$  curve shown in Fig.13 below is a vital parameter of a solar or photovoltaic cell device. The blue and orange curves are representation of the solar cell response under dark and illuminated conditions during the  $I$ - $V$  characterisation process respectively. Furthermore, the open circuit voltage ( $V_{oc}$ ) can be defined as the maximum attainable voltage of a solar cell when the current through the device is zero, resulting from the terminals being unconnected. The open-circuit voltage of a solar cell is influenced by the forward bias voltage  $V$  across the device. Another

important electrical parameter is called the short circuit current ( $I_{sc}$ ) which can be defined as the current that passes through the solar cell when the voltage  $V$  across it is reduced to zero. For an ideal solar cell, it is commonly noted that the magnitudes of the  $I_L$  and  $I_{sc}$  are equal. Hence, it may be asserted that the  $I_{sc}$  denotes the utmost magnitude of current that can be derived from a solar cell (68-69).

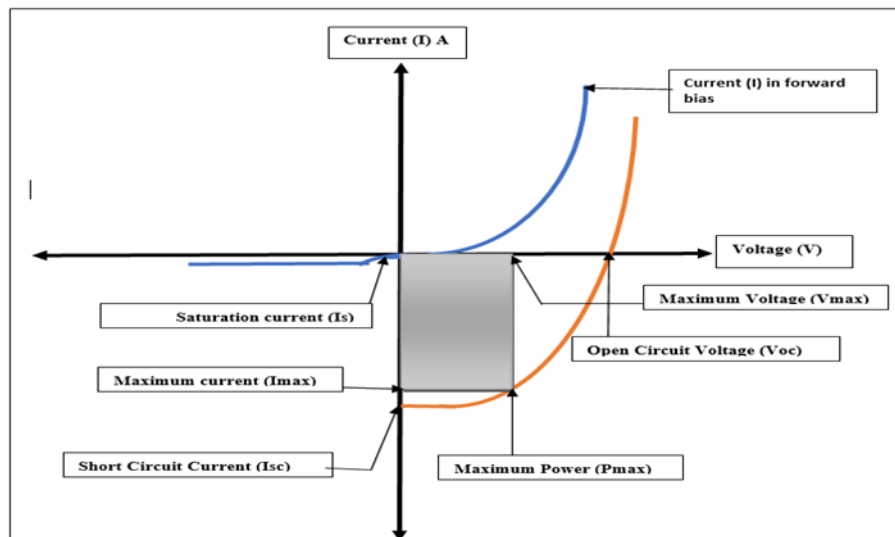


Figure 13 A typical current-voltage (I-V) curve of an ideal solar or photovoltaic cell drawn and adapted from (64) presented as a linear format

It is instructive to note that the I-V curves are also presented in semilog format as will be seen later in sections 3.3.2 and 3.3.3. Semi-log scale is useful for data with exponential relationship where one variable covers a range of values. The other important parameters that can be derived from I-V curve measurements are fill factor (FF) and solar cell efficiency ( $\eta$ ). The fill factor is a measure of the squareness of the current-voltage characteristic curve depicted by the shaded rectangular area of shown in Fig.13. In this context, the FF can be defined as the ratio of the maximum output power to the product of the  $I_{sc}$  and  $V_{oc}$  in a solar cell (69), described in the mathematical formula below:-

$$\text{Fill Factor (FF)} = \frac{I_{\max}V_{\max}}{I_{sc}V_{oc}} \quad [7]$$

Consequently, the solar cell efficiency ( $\eta$ ) can therefore be obtained from the mathematical equation seen below:-

$$\text{Efficiency } (\eta) = \frac{P_{\max}}{P_{in}} \times 100\% \quad [8]$$

$P_{in}$  is described as the input power delivered to the solar cell which is based on the total incident radiant energy on the total surface area of the solar cell which is  $1000\text{W}/\text{m}^2$  or  $100\text{mW}/\text{cm}^2$ . Its worth mentioning here, that each solar cell semiconductor absorber material area ( $A$ ) expressed in  $\text{cm}^2$  is the total surface area receiving the incident radiant energy or the product of the incident radiant energy and total surface area. For undoped In/a-Si:H/AZO-coated-glass and undoped In/SiNWs/AZO-coated-glass the total surface area ( $A$ ) measured is  $0.0177\text{cm}^2$  based on the diameter of the circular thin metal masked used in the

laboratory. The value of  $n$  of the solar cell mentioned earlier can also be determined by plotting a graph of the natural logarithm ( $\ln$ ) of the  $I$  versus the applied voltage ( $V$ ) across the solar cell in dark condition as extracted from the I-V characteristic curve measurements (69-70) and the mathematical expression to support this procedure is stated in equation 9. Thus, from equation 10, which represents the slope  $m$  of the graph, by transposing the equation, the values of  $n$  can be determined (71). The values of  $n$  for all sets of solar cell devices fabricated in this work were calculated by employing the slope of the linear region in forward bias through the process of extrapolating the point of intersection with the y-axis, particularly at the applied direct current (dc) voltage of zero when the of graph ( $\ln I$ ) is plotted against the voltage ( $V$ ) applied across these device.

$$\ln(I) = \ln(I_s) + \frac{1}{n} \left( \frac{eV}{kT} \right) \quad [9]$$

and

$$m = \frac{1}{n} \times \frac{e}{kT} \quad [10]$$

In summary, the I-V curve measurements acquired from the I-V curve in this investigation are presented in a semi-logarithmic format. In order to deduce the fill factor and the efficiency of the solar cell devices fabricated in this study. An alternate approach was implemented to compute these values which involved the utilisation of equations 11 and 12, as explored by (71), due to the exponential characteristics and apparent asymmetry observed in the graphs. Based on the findings of previous research (71), there exists a profound correlation between the  $V_{oc}$  and  $V_{max}$  parameters, as represented by a semi-empirical equation denoted as equation 11 which represents a single diode model for the fabricated devices as explained in Fig.12 above earlier in this section. Furthermore, the research conducted by (71) also demonstrates that FF is dependent on  $V_{oc}$ , exhibiting a consistent increase when the  $V_{oc}$  value increases. Moreover, the parameters  $V_{oc}$ ,  $I_{sc}$ , and  $n$  were easily derived by the analysis of the I-V characteristic curve, taking into account established constants of thermal voltage at equilibrium which is 0.0256V stated in the literature on semiconductor physics and solar cell physics (64) and (67-71).

$$FF = \frac{V_{oc} - \frac{kT}{e} \times \ln\left[\left(\frac{eV_{oc}}{kT}\right) + 0.72\right]}{V_{oc} + \frac{kT}{e}} \quad [11]$$

$$\eta = \frac{FF \times I_{sc} \times V_{oc}}{P_{in} \times A} \quad [12]$$

In the next sub-sections, the theory of band alignments and results obtained from I-V curves are presented and discussed. Its worth mentioning that the values of the rectification ratio (RR) measured in dark condition is just the ratio of the forward diode current ( $I$ ) to the diode or reverse saturation current (67).

Band diagram and current-voltage curve of In/a-Si:H/AZO-coated-glass

The undoped Schottky junction In/a-Si:H/AZO-coated-glass solar cell band diagram is drawn not to scale with the vacuum serving as the reference point is shown in Fig.14.

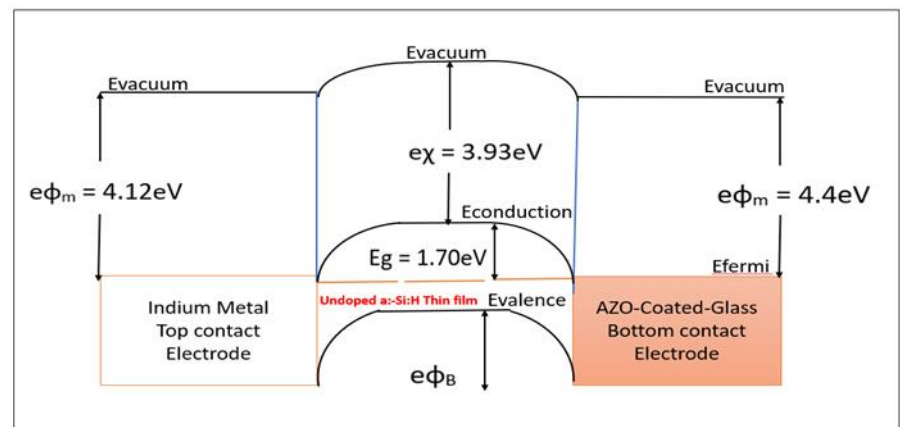


Figure.14 The band diagram of undoped Schottky junction In/a-Si:H/AZO-coated glass solar cell not drawn to scale. In/a-Si:H interface is the Schottky contact electrode, while, a-Si:H/AZO-coated-glass interface is the ohmic contact electrode.

Indium metal is used as the top contact electrode, while, AZO-coated-glass is the bottom contact electrode as represented in Fig.14 for both samples of fabricated solar cell devices. Indium metal has a work function ( $e\phi_m$ ) of approximately 4.12eV, while that of AZO-coated-glass is estimated between 4.4-4.8eV and a band gap ( $E_g$ ) is 3.4eV according to research conducted by (72-73). In this work, we have adopted the lower limit of 4.4eV for analysis. The differences between the  $\phi_m$  and sum of electron affinity ( $e\chi$ ) and  $E_g$  at the In/a-Si:H interface is higher than the difference in the  $e\phi_m$  and sum of  $e\chi$  and  $E_g$  at the a-Si:H/AZO-coated-glass interface. As such, this produces the barrier heights ( $e\phi_B$ ) of 1.51eV and 1.23eV at the In/a-Si:H and a-Si:H/AZO-coated-glass interfaces respectively. We have assumed a scenario for which undoped a-Si:H as exhibiting p-type silicon characteristics. As a consequence of this, the In/a-Si:H interface is the Schottky junction contact of the solar cell device, whereas the a-Si:H/AZO-coated-glass interface is the Ohmic junction contact electrode at the bottom (74-77). The analysis of the band alignment in Fig.14 however, appears to be in sharp contrast to research conducted by (78). They specifically observed that undoped a-Si:H exhibited n-type silicon characteristics. This is due to the introduction of unintentional oxygen doping into the lattice of undoped a-Si:H layer which causes an upward shift of the fermi level close to the conduction band (78). If this were the case, then,  $e\phi_B$  will be equal to the difference in the  $e\phi_m$  of the top and bottom contact electrodes, with respect to the  $e\chi$  of the semiconductor respectively as expressed in equation 13 below. Hence, the barrier heights will be 0.19eV at the In/a-Si:H and 0.47eV at the a-Si:H/AZO-coated-glass interfaces respectively (77-78).

The values seem to indicate interface characteristics that are diametrically opposed to those that are obtained from the measurements of the I-V characteristic curves measurement of six randomly selected In/a-Si:H/AZO-coated glass solar cell devices fabricated with ten devices on a sample are presented in Fig.15 below.

$$e\phi_B = e\phi_M - e\chi \quad [13]$$

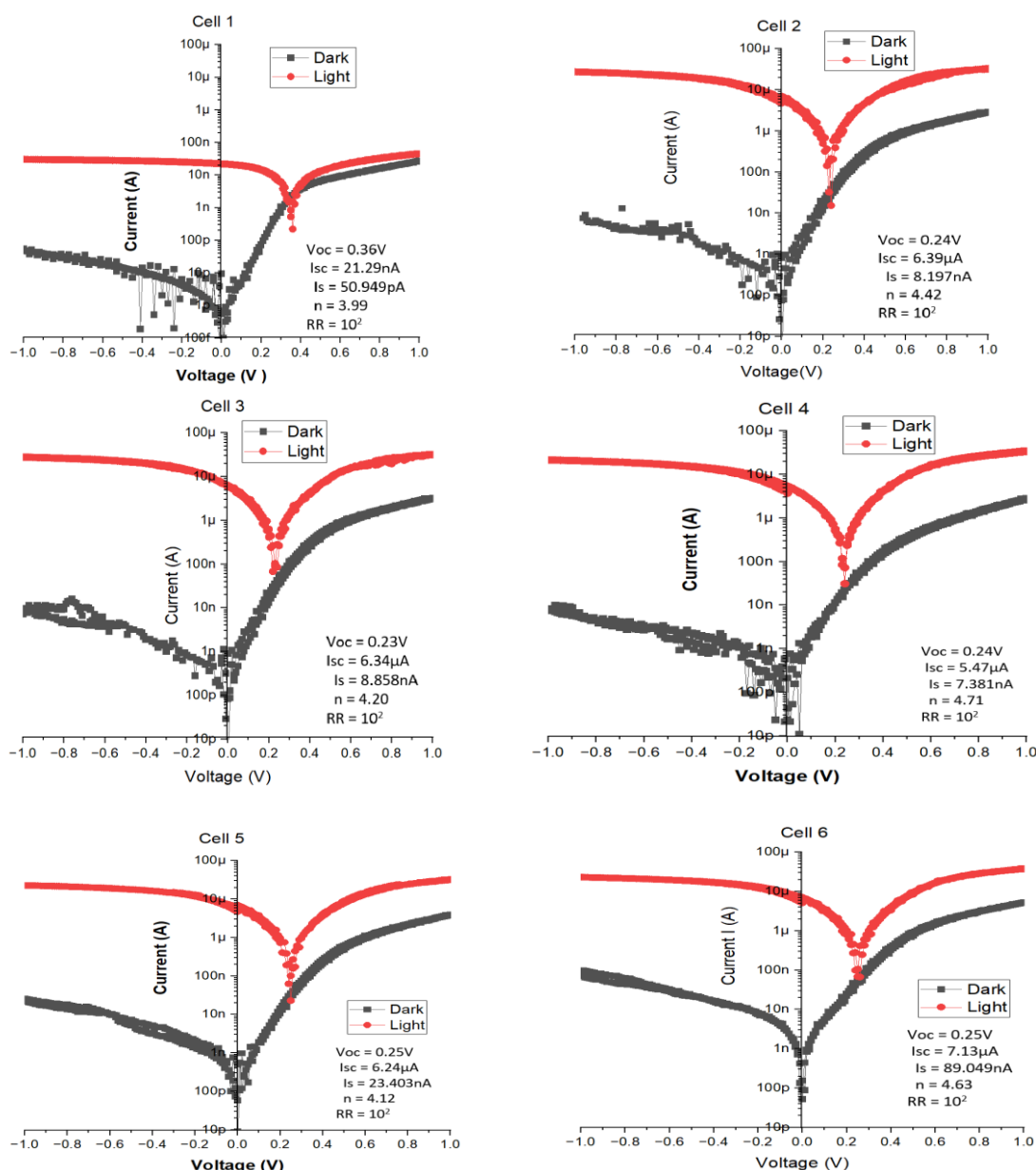


Figure.15 Shows the current-voltage (I-V) characteristic curve measurement of undoped Schottky junction In/a-Si:H/AZO-coated-glass solar cell in semi-log scale.

As observed from the I-V characteristic curve measurement in Fig.15, we notice that undoped Schottky junction In/a-Si:H/AZO-coated-glass demonstrates some diode characteristics and rectifying behaviour (76-77), with all devices having an average rectifying ratio of  $10^2$ . This diode behaviour and rectifying properties may be attributed to reduced series resistances and large shunt resistance in the undoped Schottky junction In/a-Si:H/AZO-coated glass solar cell device as a whole. It has been reported that these six devices have an average  $I_{SC}$  of  $(5.27 \pm 2.39)\mu\text{A}$ , an average  $V_{OC}$  of  $(0.26 \pm 0.04)\text{V}$ , and an average  $n$  of  $(4.35 \pm 0.26)$ . The values for the average  $V_{OC}$  obtained from the I-V characterisation measurements are in agreement with values reported in typical Schottky junction solar cell and electronic devices (75-76 and 80). Furthermore, it's suspected that the considerable contact resistance at the In/a-Si:H-interface is responsible for the low average values reported for the  $I_{SC}$  (79-80). However, under dark condition, as

indicated by the black coloured dots in the I-V curves, there appears to be a large number of trapped charge carriers. This is perhaps due to increased recombination activities within the undoped Schottky junction In/a-Si:H/AZO-coated glass solar cell device, coupled with heightened interface states phenomenon at the In/a-Si:H interface (81-83). This action of charge carrier trap states in dark seems to be in contrast to the position of Indium with respect to the middle of the silicon bandgap and minimum temperature VLS synthesised SiNWs as specified in Fig.1. The theory behind metals in relation to Silicon is that metals that are located further away from the middle band gap of silicon in Fig.1, such as, indium, gallium, aluminium metals will not form deep level traps with silicon based materials (1) and (11). This is in contrast to the case of gold located closer to silicon middle band gap and is known to form deep trap states within silicon lattice (73). On the other hand, it has been observed that under light conditions, the charge carriers have acquired sufficient kinetic and intermolecular energy to break free from the trap states in the a-Si:H layer, thereby moving into the conduction band as free charge carriers for charge extraction at the Indium top contact electrode. From the equations 11 and 12 listed earlier, the estimated efficiencies of these fabricated devices have been computed for all six devices shown in Fig.15 above. The table provided below presents a summary of the solar cell parameters for undoped Schottky junction In/a-Si:H/AZO-coated-glass solar cell devices. The values of Voc, Isc, Is, and RR have been directly derived from measurements of the I-V characteristic curve. On the other hand, the values of n, FF, and  $\eta$  were determined by a combination of I-V characteristic curve data and the use of equations 10, 11, and 12, respectively.

Table.1, the extracted solar cell/photovoltaic electrical parameters from the I-V measurements of undoped Schottky junction In/a-Si:H/AZO-coated-glass.

Open circuit voltage $V_{oc}(V)$	Short circuit $I_{sc}(\mu A)$	Dark saturation Current $I_s(nA)$	Ideality Factor (n)	Rectification Ratio (RR)	Fill Factor (FF)	Efficiency of solar cell ( $\eta$ )%
0.36	0.02129	0.05094	3.99	$10^2$	0.0754	$3.26 \times 10^{-4}$
0.24	6.39	8.197	4.42	$10^2$	0.0680	$5.89 \times 10^{-4}$
0.23	6.34	8.858	4.20	$10^2$	0.0672	$5.53 \times 10^{-4}$
0.24	5.47	7.381	4.71	$10^2$	0.0680	$5.04 \times 10^{-4}$
0.25	6.24	23.403	4.12	$10^2$	0.0688	$6.06 \times 10^{-4}$
0.25	7.13	89.049	4.63	$10^2$	0.0688	$6.92 \times 10^{-4}$

As observed from the table above, the fabricated solar cell devices investigated in this work all exhibit average  $\eta\%$  values is  $(4.78 \times 10^{-4} \pm 1.15 \times 10^{-4})$  which is rather far lower than what has been reported in previous work (61),(68),(76-78) and (84-85). This low  $\eta\%$  values which are reported is suggestive of increased recombination activities within the lattice structure of these devices. Additionally, the likelihood of the presence of metal induced gap states (MIGS) evidenced by the high values of n deduced from measurements and observed on Table 1, is perhaps a contributory factor to the low  $\eta\%$  values reported in this work. Consequently, there is a possibility the  $\eta\%$  of these devices can be improved through careful optimisation of process parameters, increasing the solar cell area, alloying with other materials and light doping (84-85). The graphs used to determine the ideality factors of the In/a-Si:H/AZO-Coated-Glass are seen in Fig.16 on the next page.

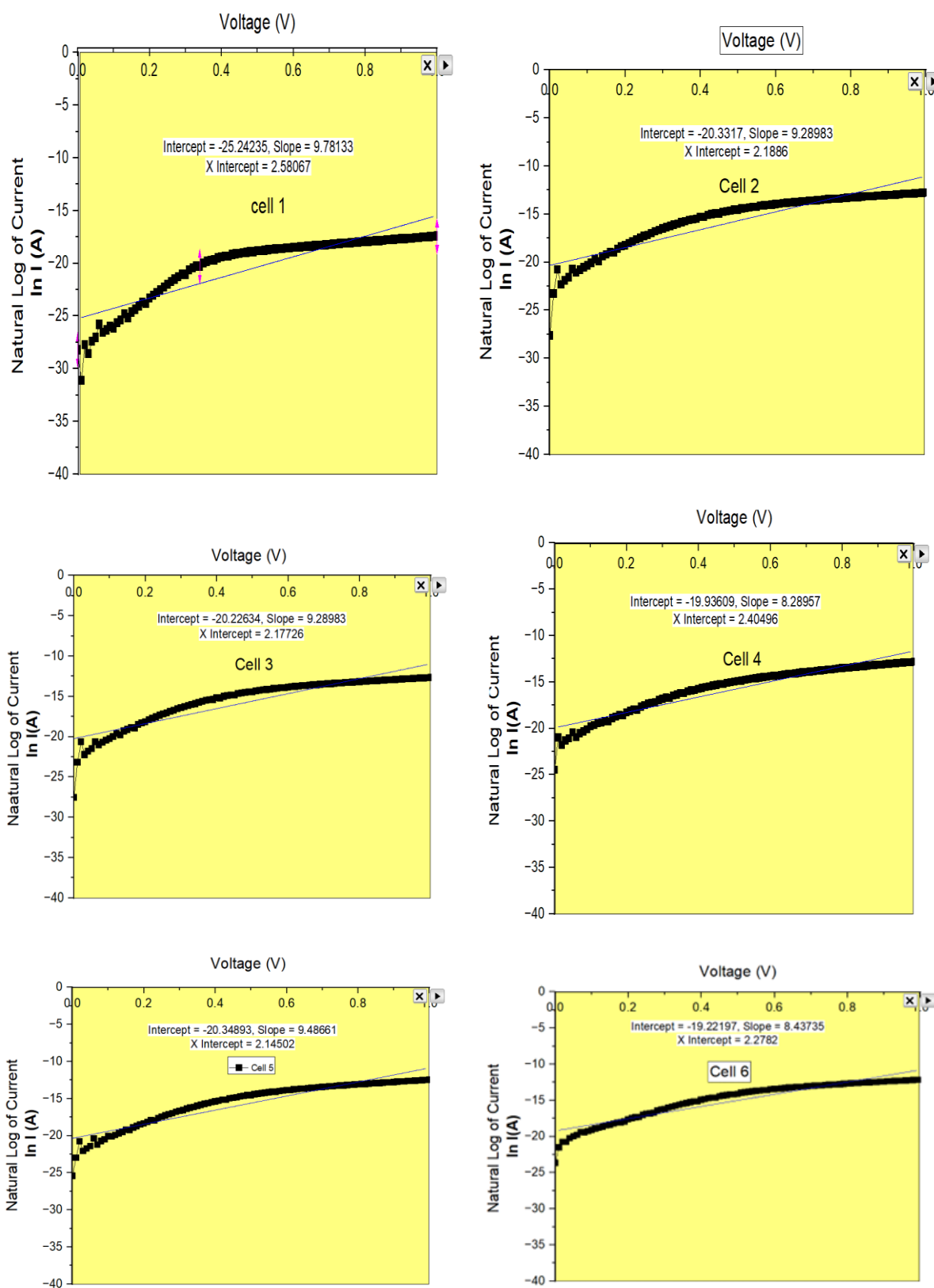


Figure.16 Shows the corresponding natural logarithm of current  $\ln I$  versus applied voltage across the undoped Schottky junction  $\text{In/a-Si:H/AZO-coated-glass}$  solar cell used to derive the ideality factors.

## Band diagram and current-voltage curve of In/SiNWs/AZO-coated-glass

The undoped Schottky junction In/SiNWs/AZO-coated-glass solar cell band diagram is drawn not to scale with the vacuum serving as the reference point are shown in Fig.17.

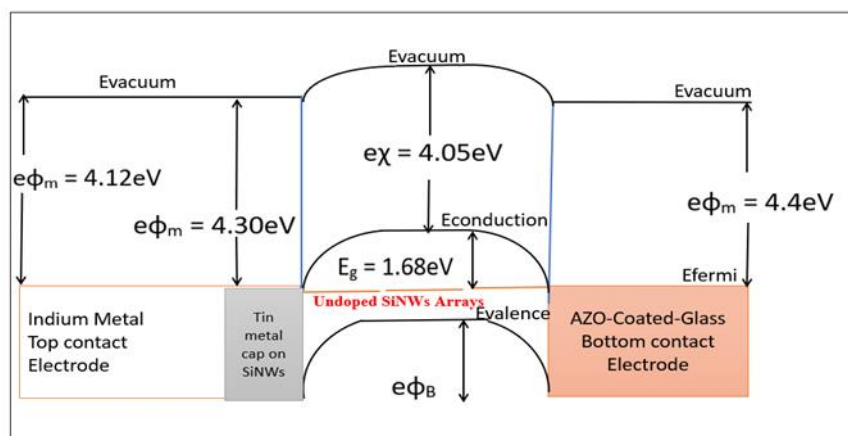


Figure.17 The band diagram of undoped Schottky junction In/SiNWs/AZO-coated glass solar cell not drawn to scale. Both In/a-Si:H and a-Si:H/AZO-coated-glass interfaces exhibit ohmic contact properties.

In spite of the fact that the difference in the sum of  $E_g$  and  $e\chi$  of the undoped SiNWs array and  $e\phi_M$  of the indium top contact electrode is 1eV higher than what was obtained with undoped a-Si:H thin film solar cells devices as observed from the I-V characteristic curve measurement in Fig15. We notice that undoped Schottky junction In/SiNWs/AZO-coated-glass demonstrates ohmic and non-rectifying junction behaviour (76-78). This is thought to be the result of fermi level pinning activities, which resulted in the introduction of MIGS into the band gap of SiNWs array (83). Furthermore, its suspected there is very high series resistance between the In/SiNWs interface as a result of the tin metal cap residue on the SiNWs arrays. Tin metal cap residue is reasoned as enhancing the formation of an Ohmic and non-rectifying junction properties in spite of the higher differences in the  $e\phi_B$  between In/SiNWs interface compared to In/a-Si:H interface. Thus,  $e\phi_B$  at the In/SiNWs and SiNWs/AZO-coated glass interfaces are 1.61eV and 1.33eV respectively. If, on the other hand, we take into account the tin metal cap residue on the SiNWs array, then the  $e\phi_B$  at the Sn/SiNWs and SiNWs/AZO-coated glass interfaces are, respectively, 1.43eV and 1.33eV. Due of the very close values of the  $e\phi_B$ , it is possible present a hypothesis that, the latter values of the barrier heights could be responsible for the ohmic and non-rectifying junction behaviour observed in the I-V characteristic curve measurements (75-82), seen in Fig.18 below. Therefore, the mathematical expression in equation 7 depicts the formular for the  $e\phi_B$  for p-type semiconductor material which has been applied to both solar cell devices investigated in this work.

$$e\phi_B = E_g + e\chi - e\phi_M \quad [7]$$

The I-V characteristic curves of six randomly selected In/SiNWs/AZO coated glass solar cell devices fabricated with ten devices on a sample are presented below in Fig.18.

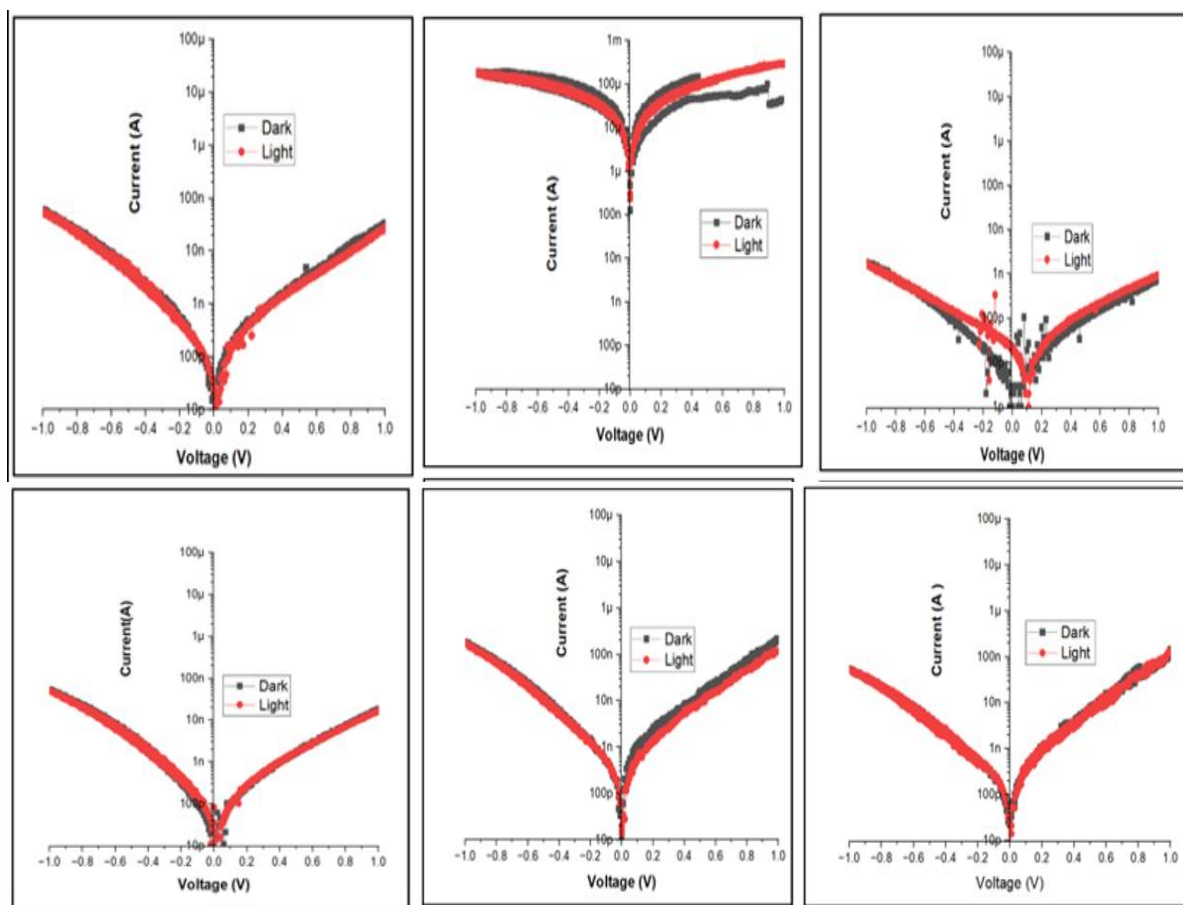


Figure.18 I-V characteristic curve measurement of undoped Schottky junction In/SiNWs/AZO-coated-glass solar cell in semi-log scale.

The measurements of the I-V characteristic curve shown in Fig.18 are ohmic and non-rectifying behaviour. Shorting out of the SiNWs array to the AZO-coated glass bottom contact electrode is reasoned to also be a major factor of this phenomenon. Additionally, it is hypothesised that there may be increased series resistance between the indium top contact electrode and the array of SiNWs caused by the residue of tin metal catalyst (86-88). Furthermore, the formation of the ohmic and non-rectifying properties observed may also be influenced by oxidation process (89-91) occurring on the surface of the SiNWs array-interface as a result of its interaction with the surrounding ambient air after removal from PECVD chamber. The efficiency values of these solar cell devices cannot be computed as they do not exhibit any solar cell rectifying characteristics. Thus, based on the fact that no pronounced solar cell behaviour and rectification properties is observed, there was no need to prepare a table of measured and computed values as seen for undoped In/a-Si:H/AZO-coated-glass in Table.1 above.

## Conclusion

In this comparative study of the electrical properties of undoped Schottky junction In/a-Si:H/AZO-coated-glass and In/SiNWs/AZO-coated-glass, the possibility of using indium as a top contact-electrode being a potential to obtaining enhanced solar cell electrical device characteristics was investigated. At this point,

it is important to note that at least ten samples of each sets of device were fabricated, and the measurements of their respective I-V characteristic curves measurements appear to have similar behaviour and good reproducibility when compared to the six samples of each device that were reported in this work. Nevertheless, despite indium's position with respect to middle band gap of silicon when considered as 1.12eV on the impurities of various metal chart. Charge carrier traps was observed in both sets of solar cell devices fabricated, which suggested some trap assisted recombination activities of charge carriers based on data recorded on the basis of information obtained from the I-V characteristics curves. Solar cell behaviour and rectifying properties were demonstrated for all In/a-Si:H/AZO-coated glass devices, based on the measured values of  $V_{OC}$ ,  $I_{SC}$ ,  $R_{SC}$ ,  $RR$  and  $n$ . The sets of undoped In/SiNWs/AZO-coated glass solar cell devices on the other hand, did not exhibit any solar cell behaviour; as a result, no meaningful solar cell data could be retrieved from the I-V characteristic curve measurements.

## Acknowledgement

Prof. Shashi Paul, the director of EMTERC and my PhD supervisor, deserves my gratitude for all the academic and professional guidance he provided throughout my studies. In addition, I would like to thank and appreciate greatly, Dr. Krishna Manjunatha for assisting me during the device fabrication process.

## References

1. Sze S.M, Physics of Semiconductor Devices, 2nd ed. Wiley, New York, 1981.
2. Maestrini A, Thomas B, Wang H, Jung C, Treuttel J, Jin Y, et al., Schottky Diode-Based Terahertz Frequency Multipliers and Mixers, *Comp. Rendus Phys.*, vol. 11, no. 7, pp. 480-495, 2010.
3. Nadri S, Moore C M, Sauber N D, Xie L, Cybery M E, Gaskins J T, et al., Thermal Characterization Of Quasi-Vertical GaAs Schottky Diodes Integrated on Silicon, *IEEE Trans. Electron Devices*, vol. 66, no. 1, pp. 349-356, 2019.
4. Kong X, Zhang L, Liu B, Gao H, Zhang Y, Yan H, et al., Graphene/Si Schottky Solar Cells: A Review of Recent Advances and Prospects, *RSC Adv.*, vol. 9, no. 2, pp. 863-877, 2019.
5. Reddy V.R, Electrical properties of Au/polyvinylidene fluoride/n-InP Schottky diode with Polymer Interlayer, *Thin Solid Films*, vol. 556, pp. 300-306, Apr. 2014.
6. Zhao B, Wang F, Chen H, Wang Y, Jiang M, Fang X, et al., Solar-Blind Avalanche Photodetector Based On Single ZnO-Ga<sub>2</sub>O<sub>3</sub> Core-Shell Microwire, *Nano Lett.*, vol. 15, no. 6, pp. 3988-3993, Jun. 2015.
7. Chang K.E, Kim C, Yoo T. J, Kwon M.G, Heo S, Kim S. Y, et al., High-responsivity Near-Infrared Photodetector using Gate-Modulated Graphene/Germanium Schottky junction", *Adv. Electron. Mater.*, vol. 5, no. 6, 2019.
8. Clemens W, "Polymer electronics" in *Technology Guide: Principles—Applications—Trends*, Berlin, Germany: Springer, pp. 84-87, 2009.
9. Hernandez-Como N, Rivas-Montes G, Hernandez-Cuevas F.J, Mejia I, Molinar-Solis J.E and M. Aleman, Ultraviolet Photodetectors Based on Low Temperature Processed ZnO/PEDOT:PSS Schottky barrier diodes, *Mater. Sci. Semicond. Process.*, vol. 37, pp. 14-18, 2015.
10. Ana R, Juan S.E, Patricia N and Antonio C.G, Less-Studied Technology-Critical Elements (Nb, Ta, Ga, In, Ge, Te) in the Marine Environment: Review on Their Concentrations in Water and Organisms. *Front. Mar. Sci.*, pp.1-9, 2019.
11. Schmidt V, Wittemann J.V, Senz S, and Goesele U, Silicon Nanowires: A Review on Aspects of Their Growth and Their Electrical Properties. *Adv. Mater.* vol. 21, pp.2681-2702, 2009.
12. J.R Davis, et.al, Impurities in Silicon Solar Cells. *IEEE Trans. Electron Devices* vol.27, pp.677-687, 1980.
13. Zhang J, Li Y, Zhang B, Wang H, Xin Q and Son A. Flexible indium-gallium-zinc-oxide Schottky Diode Operating Beyond 2.45 GHz. *Nature Communications* volume 6, pp.1-7, 2015.

14. Yang S, Martin W, Byrnes S, Conry T, Basu S, Paran D, Reichertz L, Ihlefeld J, Adamo C, Melville A, Chu Y, Yang H, Musfeldt J, Schlom J, Ager W, and Ramesh R. Photovoltaic Effects in BiFeO<sub>3</sub>. *Appl. Phys. Lett.*, vol.95 pp.1-8, 2009.
15. William R. Frensley. Chapter 1 - Heterostructure and Quantum Well Physics. *VLSI Electronics Microstructure Science*, vol.24, pp1-24,1994.
16. Keller J, Stolt L, Donzel-Gargand O, Kubart T, and Edoff M. Wide-Gap Chalcopyrite Solar Cells with Indium Oxide-Based Transparent Back Contacts. *RRL Solar Publications*, pp.1-13, 2018.
17. Kim H, Park M, Kim S, Park S, Song J, Kim H, Choi W and Park J. Indium-tin-oxide/GaAs Schottky Barrier Solar Cells with Embedded InAs Quantum dots. *Thin Solid Films*, vol.604, pp.81-84, 2016.
18. Wu Z, Duan W, Lambertz A, Qiu A, Pomaska M, Yao Z, Rau U, Zhang W, Liu Z and Ding K. Low-resistivity p-type a-Si:H/AZO Hole Contact in High-Efficiency Silicon Heterojunction Solar Cells. *Applied Surface Science*, vol.542, 2021.
19. Lee S, Choi H, Li H, Ji K, Nam S, Choi J, Ahn S, Lee H and Par B. Analysis of a-Si:H/TCO Contact Resistance for the Si Heterojunction Back-Contact Solar Cell. *Solar Energy Materials and Solar Cells*, vol.120, pp.412-416, 2014.
20. Kim S, Jung J, Lee Y, Ahn S, Hussain S, Park J, Song B, Han S, Dao V, Lee J, and Yi J. Role of double ITO/In<sub>2</sub>O<sub>3</sub> Layer for High Efficiency Amorphous/Crystalline Silicon Heterojunction Solar Cells. *Materials Research Bulletin*, vol.58, pp.83-87, 2014.
21. Shin C, Mohseni K, Yu K, Tomasulo S, Montgomery K, Lee M, Rogers J, and Li X. Heterogeneous Integration of InGaAs Nanowires on the Rear Surface of Si Solar Cells for Efficiency Enhancement. *ACS Nano*, vol.6, pp.11074–11079, 2012.
22. McPheeters C and Yu E. Computational Analysis of Thin Film InGaAs/GaAs Quantum Well Solar Cells with Back Side. Light Trapping Structures. *Opt. Express* pp.864-878, vol.20, 2012.
23. Trevor M. Letcher. Photoelectrical Efficiency. *Comprehensive Renewable Energy*. Elsevier Ltd, pp.1-256, 2022.
24. Kessel E. Remote Plasma Deposition of Hydrogenated Amorphous Silicon. *Plasma Processes, Film Growth and Material Properties*. Eindhoven University of Technology, pp.1-8, 2000.
25. Bhandaru S, Bozzola A, Liscidini M and Sharon M. Weiss Efficiency Enhancement via Metal-Coated Porous Amorphous Silicon Back Reflectors Incorporated In Amorphous Silicon Solar Cells. *MRS Communication*, 2016.
26. Go B, Kim D, Oh S, Kim C, Choi H and Lee H. Improved Conversion Efficiency of Amorphous Si Solar Cells Using A Mesoporous ZnO Pattern. *Nanoscale Research Letters* vol.9, 2014.
27. Beatriz Santos. Hydrogenated Amorphous Silicon Solar Cell for BIPV, Bifacial Applications. *PV Magazine*, South Korea's Institute of Materials Science, 2023.
28. Chen D, Liu S, Liu Y, He C and Yin P: Study on Uniformity Control of Amorphous Silicon Thin Films by PECVD. School of Optoelectronic Information, University of Electronic Science and Technology of China; Chengdu Yanbai Technology Co.Ltd.
29. Wilfred G.J, et.al, Methods of Deposition of Hydrogenated Amorphous Silicon for Device Applications. *Thin Films and Nanostructures*. Science Direct, vol. 30, pp.1-215, 2002.
30. Kasap S and Capper P, *Transparent Conductive Oxides*, Springer Handbook of Electronic and Photonic Materials, pp.1391-1403, 2017.
31. Nemanich R.J, *Semiconductors and Semimetals*, Academic Press, Orlando, p.375, 1984.
32. Hosono H, et.al, *Handbook of Transparent Conductors*. Springer books, Berlin, 2011.
33. Chen I and Lee S: Proceedings of the 9th International Conference on Amorphous and Liquid Semiconductors. *Journal of Physics*. pp.1045, 1982.
34. Martins R, Ferreira L, Carvalho C.N, Maçarico A and Guimarães L: Amorphous Silicon Technology. Department of Materials Science, Faculty of Science and Technology of New University of Lisbon, Portugal. pp.153-158, 1982.
35. Martins R, Ferreira L, Carvalho C and Guimarães L, *Journal of Non-Cryst. Solids*, pp.137-138 and pp.757-760, 1991.
36. Luderer C, et.al, Contact Resistivity of TCO/a-Si:H/c-Si Heterojunctions. Presented at the 36th European PV Solar Energy Conference and Exhibition, Marseille, France 2019.
37. Crose M, Kwon J, Nayhouse M, Ni D and Christofides P. On Operation of PECVD of Thin Film Solar Cells. *IFAC-Papers Online*, vol. 48, pp.278-283, 2015.
38. R.S.Wagner and W. C.Ellis, Vapour-Liquid-Solid Mechanism of Single Crystal Growth, *Appl. Phys.*, vol. 4, pp. 89-90, 1964.
39. Givargizov E.I, Fundamental Aspects of VLS Growth, *Journal of Crystal Growth*, vol.31, pp.20-30, 1975.
40. Bootsma G.A and Gassen H.J. Quantitative Study on the Growth of Silicon Whiskers from Silane And Germanium Whiskers From Germane. *J. Crystal Growth*, vol.10, pp.223-234, 1971.
41. S Misra, Yu L, Chen W, Foldyna M and Cabarocas P. , A Review of The Plasma Assisted VLS Synthesis of Silicon Nanowires and Radial Junction Solar Cells, *Journal of Physics D*, vol. 47, pp.1-20, 2014.

42. Goldstein J, Newbury D, Echlin P, Joy D, Lyman C, Lifshin E, Sawyer L and Michael R. Scanning Electron Microscopy and X-ray Microanalyses, 3rd edition. New York: Plenum Press, 2003.
43. Thinky Library, Evaluation of Materials using Scanning Electron Microscope (SEM) Technical Report, [Internet]. 2018 [cited 2023 July,15] Available from: <https://www.thinkymixer.com/en-gl/library/report/evaluation-of-materials-using-scanning-electron-microscope-sem>.
44. Tauc, J : Optical Properties of Solids Edited by Abeles, F . North-Holland Publication Co, pp277-313, 1972.
45. Hama T, Okamoto H, Hamakawa Y and Matsubara T, Hydrogen Content Dependence of the Optical Energy Gap in Hydrogenated Amorphous Silicon Journal on Crystalline Solids, vol. 133, pp.59-60. 1983.
46. Pankove J.I and Carlson D.E, Electrical and Optical Properties of Hydrogenated Amorphous Silicon. Annual Review of Materials Science, vol.10, pp.43-63, 1980.
47. Bao H, Optical Absorption Enhancement in Disordered Vertical Silicon Nanowire Arrays for Photovoltaic Applications. Optical Letters, vol.35, pp.3378-3380.2010.
48. Zhong H, Anran G, Guohui G, Lei W, and Jiang Y, The Enhanced Light Absorbance and Device Application of Nanostructured Black Silicon Fabricated by Metal-Assisted Chemical Etching Nanoscale Research Letters.vol.11, pp.1-6, 2016.
49. Street R.A, William S.W and Christopher P, Analytic Model for Diffuse Reflectivity of Silicon Nanowire Mats. Nano Letters, vol.9, pp.3494-3497, 2009.
50. Tauc J.et.al, Optical Properties and Electronic Structure of Amorphous Germanium”, Physica Status Solidi, B, 1996.
51. Adachi M, Anantram M and Karim K. Core-Shell Silicon Nanowire Solar Cells. Scientific Reports, pp.1-6, 2013.
52. Rech, R. and Wagner, H. Potential of Amorphous Silicon For Solar Cells. Appl. Phys. vol.69, pp.155-167, 1999.
53. Whittig L, and Allardice W, X-Ray Diffraction Techniques Methods of Soil Analysis, Part 1: Physical and Mineralogical Methods, American Society of Agronomy, Madison, pp.331-362. 1986.
54. Russ J, Fundamentals of Energy Dispersive X-ray Analysis: Butterworth-Heinemann, 1984.
55. Technology Networks, Analysis and Separations. UV-Vis Spectroscopy: Principle, Strengths and Limitations and Applications, [Internet]. 2023 [cited 2023 July,20]. Available From: <https://www.technologynetworks.com/analysis/articles/uv-vis-spectroscopy-principle-strengths-and-limitations-and-applications>.
56. Shawn Willis. Advanced Optoelectronic Characterisation of Solar Cells. Oriel College, A Thesis Submitted for the Degree of D-Phil in Materials University of Oxford. Chapter 1, p.6, 2011.
57. Cromwell C and Sze S. Current Transport in Metal Semiconductor Barriers, Solid State Electron, vol.9, pp.1035-1048, 1966.
58. Vidhya Chakrapani. Semiconductor Junctions, Solid-Solid Junctions. Encyclopaedia of Applied Electrochemistry vol.1, pp.1882-1887, 2014.
59. Feroz A and Hossain F. Influence of Front and Back Contacts on Photovoltaic Performances of P-N Homo-Junction Silicon Solar Cell, International J. of Photo-Energy, pp.1-6, 2017.
60. Wolf S, Descoedres A, Holman Z, Barraud L, Morel S and Ballif C. 21% Efficient Silicon Heterojunction Solar Cells on n-type and p-type Silicon Wafers Compared, 2013.
61. Mikolášek M, Silicon Heterojunction Solar Cells: The Key Role of Hetero-interfaces and their Impact on the Performance Nanostructured Solar Cells. pp.69-92, 2016.
62. Zebin L, Zhonghang W, Jiaqi J, Kongduo H, Zhenliu C, Xilu Y, Hang Y, Qiongrong O and Rongqing L. Enhanced Work Function of Al-Doped Zinc-Oxide Thin Films by Oxygen Inductively Coupled Plasma Treatment, Plasma Science and Technology, vol.16, pp.79-82, 2014.
63. Tsay C.Y and Hsu W.T. Comparative Studies on Ultraviolet-Light-Derived Photo Response Properties of ZnO, AZO, And GZO Transparent Semiconductor Thin Films, .PMC .Materials, Vol. 10, pp.1-12, 2017.
64. Keithley, Application Note Series. Making I-V and C-V Measurements on Solar/Photovoltaic Cells Using the Model 4200-SCS Semiconductor Characterisation System. [Internet]. 2007 [cited 2023 July,22]. Available From: <https://studylib.net/doc/making-i-v-and-c-v-measurements-on-solar-photovoltaic-cells>.
65. Cotfas D.T: Methods and Techniques to Determine the Dynamic Parameters of Solar Cells: Renewable and Sustainable Energy Reviews, vol.61, pp.213-221, 2016.
66. Tom Markvart and Luis Castañer. Practical Handbook of Photovoltaics 2nd Edition. Chapter IA-1 - Principles of Solar Cell Operation. Elsevier. pp.7-31, 2012.
67. Sze M and Kwok N, Physics of Semiconductor Devices 3rd Edition. New Jersey: Wiley, 1981. pp.134-170.
68. Solar Cells/Modules. Solar World Expo. [Internet]. 2022 [cited 2023 July,22]. Available From: <https://www.pvresources.com/en/solarcells/solarcells.php>.
69. Martin A. Green. Accurate Expressions for Solar Cell Fills Factors Including Series and Shunt, Applied. Physics. Letters, vol.108, 2016.

70. Goetzberger A, Hebling C and Schock W. Photovoltaic Materials, History, Status and Outlook, Materials Science and Engineering: R: Reports, vol. 40, pp.1-46, 2003.
71. Jeffery .L. Gray. The Physics of Solar Cell. Chapter 3.A Handbook of Photovoltaic Science and Engineering, 2nd Edition Indiana, pp.83-129. 2011.
72. Corpus-Mendoza A.S, De Souza M.M and Hamelmann F .Transport Mechanisms and Effective Schottky Barrier Height of ZnO/a-Si:H and ZnO/ $\mu$ c-Si:H Heterojunction Solar Cells. Journal of Applied Physics, vol.114, pp.184505-1 -184505-6, 2013.
73. G Drewelow, Reed A, Stone C, Roh K, Jiang C.T, Thi-Truc L.N, Noh H, Park H and Lee S. Work Function Investigations on Al-doped ZnO for Band-Alignment in Electronic and Optoelectronic Applications. Applied Surface Science, vol.484, pp.990-998, 2019.
74. Suche M, Christoulakis S, Katsarakis N, Kitsopoulos T. and Kiriakidis G. Comparative Study of Zinc Oxide and Aluminium Doped Zinc Oxide Transparent Thin Films Grown by Direct Current Magnetron Sputtering. Thin Solid Films, vol.16, pp.6562-6566, 2007.
75. Tung R.T. The Physics and Chemistry of the Schottky Barrier Height. Applied Physics Reviews vol1, pp.11304-11354, 2014.
76. Schropp R and Zeman M, Amorphous and Microcrystalline Silicon Solar Cells. Modelling, Materials and Device Technology. Kluwer Academic Publishers, pp.44-45, 1998.
77. Kelly M, Todd G, Sisson J and Wickenden K. Contacts Between Amorphous Metals and Semiconductors Electronics Letters, 1983
78. Mikolášek M, Jakaboviš J, Andok R, Řeháček V and Harmatha L, Capacitance Analysis of the Structures with the a-Si:H(i)/c-Si(p). Heterojunction for Solar-Cell applications, Journal of Electrical Engineering, vol.65, pp. 254-258, 2014.
79. Laughton, M. A. Chapter 17. Power Semiconductor Devices". Electrical engineer's Reference Book. Newness. pp.25-27. 2011.
80. Holman Z, Descoendres A, Barraud L, Seif J, Zicarelli F, De Wolf S and Baliff C. Increasing Short-Circuit Current in Silicon Heterojunction Solar Cells. Conference Record of the IEEE Photovoltaic Specialists Conference, 2011.
81. Ofunoye B, Lee J, Yan M, Sun C, Zuo J.M and Adesida I. Electrical and Microstructural Properties of Thermally Annealed Ni/Au and Ni/Pt/Au Schottky Contacts on AlGaIn/GaN heterostructures. Semiconductor Science and Technology. Semicond. Sci. Technol, vol.29 pp.1-2, 2014.
82. Ukauskas H.D and Gavriushin V. The Metal-Semiconductor Junction. Schottky Diode and Ohmic Contacts. Vilnius Universities Semiconductor Physics. Department of Physics, pp1-5, 2002.
83. Islam R, Nazif N and Saraswat K. Optimization of Selective Contacts in Si Heterojunction Photovoltaic Cells Considering Fermi Level Pinning, IEEE Transactions on Electron Devices, vol.63, pp.4788-4795, 2016.
84. Bauer S, Herbst W, Schroder B and Oechsner H. a-Si:H Solar Cell using the Hotwire Technique-How to Exceed Efficiencies of 10% Proc. 26th IEEE PVSC, Anaheim, CA pp.719-722, 1997.
85. Hattori Y, Kruangam D, Katoh K, Nitta Y, Okamoto H and Hamakawa Y. High Conductivity Wide-Band Gap p-type a-Si:C:H Prepared by ECR-CVD and its application High efficiency a-Si Basis Solar Cells. Proc.19th IEEE PV Specialist Conference, pp.689-694, 1987.
86. Djoumi S, Kail F, Cabarrocass P and Chehed L. Tin Versus Indium Catalyst in the Growth of Silicon Nanowires By Plasma Enhanced Chemical Vapor Deposition on Different Substrates. Thin Solid Films, vol.758, 2022.
87. Fabiano Corsetti and Arash Mostofi, Gold Defects in Silicon Negative-U Properties For Substitutional Au in Si, Euro physics Letters vol.105, pp.57006, 2014.
88. Minsung Joen and Koichi Kamisako. Synthesis and Characterization of Silicon Nanowires using Tin Catalyst For Solar Cells Application. Materials Letters, vol.63, pp.777-779, 2009.
89. Palmstrøm C.J, Contacts for Compound Semiconductors: Ohmic Type. Encyclopedia of Materials: Science and Technology (Second Edition). pp.1581-1587, 2001.
90. Portland State. The Laboratory of Nanoelectronics/Solar Cells. [Internet]. 2017 [cited 2023 Jan 7]. Available from: <https://www.pdx.edu/nanoelectronics/solar-cells>
91. Stelzner T, Pietsch M, Andra G, Falk F, Ose E, and Christiansen S. Silicon Nanowire-Based Solar Cells. Institute of Photonic Technology, Max-Planck-Institute of Microwave structure Physics, Weinberg, Germany, pp.1-3, 2018.